JACS
JOURNAL OF THE AMERICAN CHEMICAL SOCIETY

Communication

pubs.acs.org/JACS

Atomic Structure of Self-Assembled Monolayer of Thiolates on a Tetragonal Au_{92} Nanocrystal

Chenjie Zeng,[†] Chong Liu,[‡] Yuxiang Chen,[†] Nathaniel L. Rosi,[‡] and Rongchao Jin*[,†]

[†]Department of Chemistry, Carnegie Mellon University, Pittsburgh, Pennsylvania 15213, United States
[‡]Department of Chemistry, University of Pittsburgh, Pittsburgh, Pennsylvania 15260, United States

Supporting Information

ABSTRACT: Unveiling the ligand binding mode on the crystalline surfaces is important for deciphering the long-standing structural enigma in self-assembled monolayers (SAMs). Here, the binding and patterning structures of thiolates (SR) on the Au(100) crystalline facet are revealed on the basis of the atomic structure of a highly regular, single crystalline $Au_{92}(SR)_{44}$ nanocrystal. The six exposed facets of this tetragonal nanocrystal give rise to six pieces of "nanoSAMs". We found that thiolates bind to the planar (100) facets of the nanocrystal via a simple bridge-like mode and are assembled into an overlayer with c(2 × 2) symmetry. The Au−S binding mode and translational symmetry in the kernel and on the surface of the Au_{92} nanocrystal can be generalized infinitely to construct the bulk two-dimensional SAMs and various tetragonal nanocrystals.

Self-assembled monolayers (SAMs) of thiolates on gold surfaces are an important platform for nanotechonology and are widely applied in nanolithography, molecular monolayer junction, sensors, and biomedicine, to name a few.[1−4] However, the atomic structures of SAMs, including the nature of Au−S bonds and their patterning modes, still remain elusive.[5] Surface characterization techniques in combination with theoretical calculation are the common approach to decipher the structural enigma of SAMs, and significant progress has been made in the past 30 years.[6−9]

Recently, the advancements in atomically precise thiolate-protected gold nanoclusters (denoted as $Au_n(SR)_m$) open up an opportunity to study the SAM structure on the surfaces of nanoparticles. Total structures of $Au_n(SR)_m$ nanoclusters containing tens to hundreds of gold atoms have been determined by X-ray crystallography.[10] It was found that the surfaces of gold nanoclusters are protected by ubiquitous $Au_x(SR)_{x+1}$ oligomeric staple-like motifs,[10,11] which to some extent support the Au-adatom based −S(R)−Au−S(R)− binding mode in SAMs.[12,13] For smaller-sized gold nanoclusters, longer staple motifs are generally required in order to accommodate the increasing surface curvature.[14−16] The staple motifs eventually close up and evolve into an octameric $Au_8(SR)_8$ ring motif in the $Au_{20}(SR)_{16}$ nanocluster.[17] For the larger-sized $Au_{130}(SR)_{50}$ and $Au_{133}(SR)_{52}$ nanoclusters,[18,19] their extended, curved surfaces are found to be exclusively protected by −S−Au−S− staple motifs, which are further self-aligned and assembled into ripple-like or helical stripe patterns. Such stripe patterns are reminiscent of the rectangular stripes observed in the Au(111) SAMs.[20,21]

Despite these advances, there are still some open questions when applying a three-dimensional (3D) nanoparticle structure to represent a typical 2D SAM structure:[22−25] (i) Does the self-assembly behavior of thiolates on the planar crystalline surfaces share the same rules with the curved surfaces of nanoparticles? (ii) Would the boundary effects (e.g., edges and corners) of nanoparticles affect the self-assembly process on the surfaces? To answer these questions, it is highly desirable to obtain a gold nanocluster that exposes *planar* and *extended* crystalline facets, since the *planar* feature can eliminate the influence of surface curvature, and the *extended* feature can help distinguish facet binding from edge and vertex bindings of ligands.

Here, our continuous efforts have culminated in a highly regular, tetragonal-shaped $Au_{92}(SR)_{44}$ nanocrystal, which bears flat and extended crystalline {100} facets (i.e. the "nanoSAMs"). The achievement of atomic resolution in the structure of Au_{92} nanocrystal provides insights into the structural enigma of SAMs on Au(100), including the detailed binding geometry, patterning symmetry, and assembly strategy. The differences and similarities among the binding modes of facets, edges, and corners are also revealed in the Au_{92} nanocrystal. We further generalize the rules of kernel construction and surface protection in $Au_{92}(SR)_{44}$ to the prediction of new magic-sized tetragonal nanocrystals.

The $Au_{92}(SR)_{44}$ nanocrystal, where SR = 4-*tert*-butylbenzenethiolate (TBBT), was synthesized by a two-step size-focusing method with a careful control of reaction kinetics (see Supporting Information for details). Briefly, in the first step, a mixture of $Au_x(TBBT)_y$ nanoclusters was synthesized by the controlled reduction of Au(I)−TBBT complexes. In the second step, successive size-focusing processes with excess TBBT thiol led to the accumulation of $Au_{92}(TBBT)_{44}$ nanocrystals. The formula of the final, highly stable $Au_{92}(TBBT)_{44}$ was determined by electrospray ionization mass spectrometry (ESI-MS), with the experimental molecular weight (25 391.3 Da) matching well with the theoretical value of 25 392.8 Da (Figure S1). The optical absorption spectrum of $Au_{92}(TBBT)_{44}$ shows multiple peaks at 440, 660, and 850 nm (Figure S2). Dark rhombic plate shaped single crystals of $Au_{92}(TBBT)_{44}$ were obtained by vapor diffusion of acetonitrile into a toluene solution of the nanocrystals.

Received: May 10, 2016
Published: June 29, 2016

DOI: 10.1021/jacs.6b04835
J. Am. Chem. Soc. 2016, 138, 8710−8713

X-ray crystallographic analysis shows that the kernel of $Au_{92}(TBBT)_{44}$ is a tetragonal-shaped crystallite, which can be carved out from the face-centered-cubic (fcc) lattice along the three ⟨100⟩ directions. This tetragonal crystallite is labeled as 6 × 6 × 5 to indicate the six (100) layers, six (010) layers, and five (001) layers along the *x*-, *y*-, and z-axis, respectively (Figure 1A). A total of 90 gold atoms are required to assemble into this

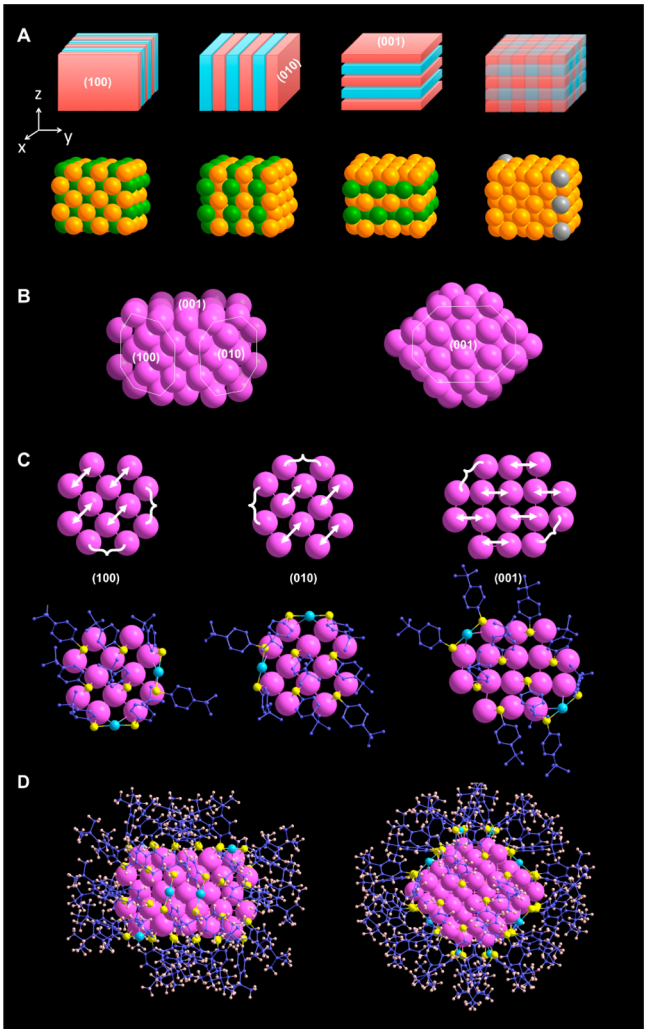

Figure 1. Structural dissection of $Au_{92}(TBBT)_{44}$ nanocrystal: (A) structural model of the gold kernel; (B) the Au_{84} kernel viewed along the [110] direction (left) and [001] direction (right); (C) binding and patterning structures of thiolates on the {100} facets; (D) total structure viewed along [110] and [001] directions. Yellow = S; purple = C; pink = H; other colors = Au. Arrows = bridging thiolates; braces = monomeric staple motifs.

1.05 × 1.05 × 0.84 nm^3 nanocrystal. Further truncation of two columns of atoms at two edges along the *z*-axis (Figure 1A, gray balls) leads to a Au_{84} kernel. Compared with the standard fcc-lattice, the Au_{84} kernel is slightly expanded (by 6%) along the $[1\bar{1}0]$ direction (Figure S3).

The highly regular Au_{84} crystallite exposes the hitherto largest crystalline {100} facet observed in the X-ray structures of gold nanoclusters. It exhibits 16-gold-atom (001) facets and 12-gold-atom (100) and (010) facets (Figure 1B,C). These six facets give rise to six pieces of "nanoSAMs". Significantly, all six facets follow the same binding and patterning modes, that is, each thiolate simply bridges two adjacent surface gold atoms (Figure 1C, arrow), and all the sulfur atoms of the thiolates align orderly to form an overlayer with square symmetry, which is commensurate to the underlying Au{100} lattice. The carbon tails of the TBBT ligands have a nearly parallel alignment. The pairing of Au atoms by bridging thiolate on the {100} facets leads to some leftover gold atoms at the edge sites, and these gold atoms are protected by additional −S(R)−Au−S(R)− staple motifs (Figure 1C, braces).

In addition to facets, it is also important to examine the thiolate protecting modes at the edges and corners of the tetragonal $Au_{92}(TBBT)_{44}$ nanocrystal (i.e., the boundary effect). As shown in Figure S4, the corner-site can be viewed as protected by −S−Au−S−Au−S− dimeric staple motif, which is actually assembled from three simple bridging thiolates at the three joining facets. Similarly, the edge is protected by −S−Au−S− monomeric staple motifs, and they can be decomposed into two bridging thiolates at the two connecting facets. It is worth noting that in the previously reported smaller fcc structures such as $Au_{36}(SR)_{24}$ and $Au_{52}(SR)_{32}$, some of the observed monomeric and dimeric staples actually correspond to the bridging thiolates at the edge and corner sites, respectively.[26,27] But due to their smaller sizes, the surface, edge, and corner sites are mixed and hard to distinguish.

The boundary effect also leads to chirality in the Au_{92} nanocrystal, and two chiral isomers can be identified in the unit cell (Figure S5). The sulfur bridges lean either to the right (/) or to the left (\) against the diamond-tiling Au(100) facets. The same orientation is adopted throughout the six facets in the Au_{92} nanocrystal. In this way, the bridging thiolates at the edges and corners are smoothly linked into the staple motifs, and the requirement of linear coordination in −S(R)−Au−S(R)− can be met (Figure S4).

Based on the binding modes and translational symmetry observed in the six pieces of nanoSAMs, we further deduced the structure of bulk Au(100) SAMs (Figure 2). The sulfur

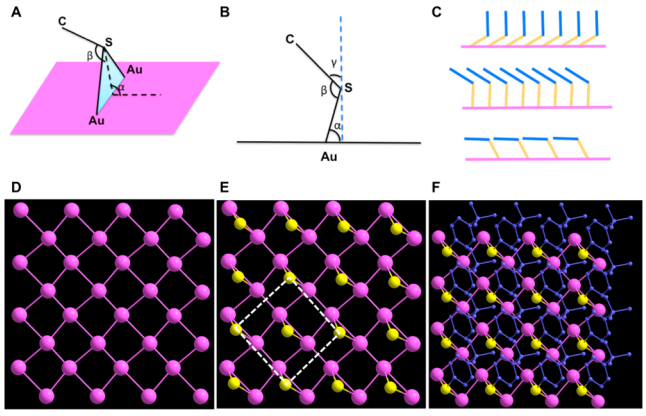

Figure 2. Binding and patterning of thiolates on Au(100) surface. (A, B) the geometric structure of the −S− bridging bond; (C) orientation of carbon tails from standing-up to lying-down positions; (D) Au lattice; (E) Au−S interface; (F) overall structure.

overlayer has 50% coverage, with one thiolate covering two gold atoms at the 2-fold bridging site. The overall patterning symmetry is c(2 × 2), with the shortest sulfur to sulfur spacing being ~4.3 Å (Figure 2E). Such a square symmetry is consistent with the earlier results based on low-energy electron diffraction (LEED),[28,29] but LEED could not assign the sulfur binding sites.

DOI: 10.1021/jacs.6b04835
J. Am. Chem. Soc. 2016, 138, 8710−8713

The detailed geometry of the −S(R)− bridging bond provides insights into the rigidity and flexibility in the SAM structure. For example, the Au−S bond length is fixed at 2.35 ± 0.05 Å, and the Au−S−Au angle is 87° ± 5°, as averaged from the 28 bridging thiolates in $Au_{92}(TBBT)_{44}$. This gives rise to the span of underneath Au−Au atoms of ∼3.2 Å, longer than the Au−Au bond in bulk gold (2.88 Å). Therefore, the underlying Au lattice in (100) SAMs is slightly reconstructed (Figure 2D), that is, the Au−Au bonds beneath the sulfur bridges are stretched, while the adjacent Au−Au bonds become contracted.[30]

The main freedom left in the Au−S bond is the dihedral angle (α) between the Au−S−Au plane and the Au lattice (Figure 2A,B). It determines the position of S atoms against the Au lattice: either in the 2-fold bridge sites ($\alpha = 90°$) or leaning toward the 4-fold hollow sites ($\alpha \neq 90°$, Figure 2E). The α angle also controls the spacing and interaction between carbon tails, as reflected in the relationship of $\gamma = 90° + \alpha - \beta$, where β is the angle between the C−S bond vector and the Au−S−Au plane, with a relatively fixed value of 120° ± 6°, and γ is the tilt angle between the carbon tails and the plane normal (Figure 2B). For example, when α is adjusted from ∼30° to ∼120° (Figure 2C), the carbon tails move from a standing-up position ($\gamma = 0°$) into a lying-down position ($\gamma = 90°$), and correspondingly the space between carbon tails shrinks. Such an adjustment is also reflected in the nanoSAMs where the boundary effect exists. The bridging thiolates at the edge sites have a larger α (∼90°), making the carbon tails tilt down to fill the extra volume at the edge sites; while the thiolates at the center of the surface tend to adopt smaller α (∼70°), so that the carbon tails tilt up to avoid the surface tension (Figure 3). The flexibility in dihedral angle makes it possible to regulate the interactions (attraction and repulsion) among the carbon tails during the self-assembly process.

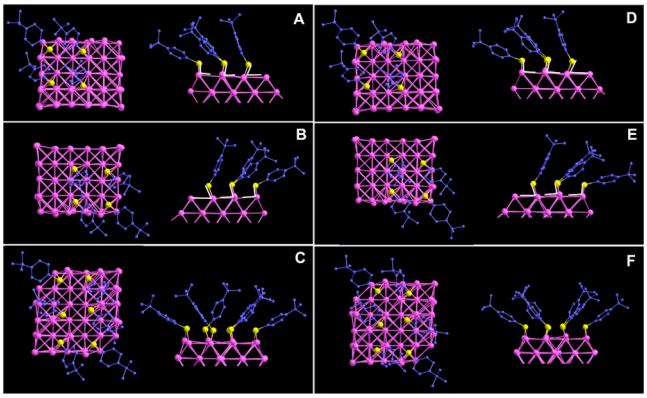

Figure 3. Structures of six "nanoSAMs" in the $Au_{92}(TBBT)_{44}$ nanocrystal: (A) (100) facet; (B) (010) facet; (C) (001) facet; (D) $(\bar{1}00)$ facet; (E) $(0\bar{1}0)$ facet; (F) $(00\bar{1})$ facet.

The kernel construction manner, surface binding and patterning modes, as well as the edge and corner protecting modes revealed by the $Au_{92}(TBBT)_{44}$ can also be generalized to fabricate different-sized tetragonal nanocrystals. Figure 4 provides three examples of expanded tetragonal nanocrystals. (i) The nanocrystal grows along the z-axis to form a 1D rod. The (n, m) for $Au_n(SR)_m$ follows the $(18k + 2, 6k + 14)$ values, where k indicates the number of atomic layers along the extending direction (e.g., z-axis in this case, Figure 4A). (ii) Expansion proceeds along both the x and y axes, forming 2D

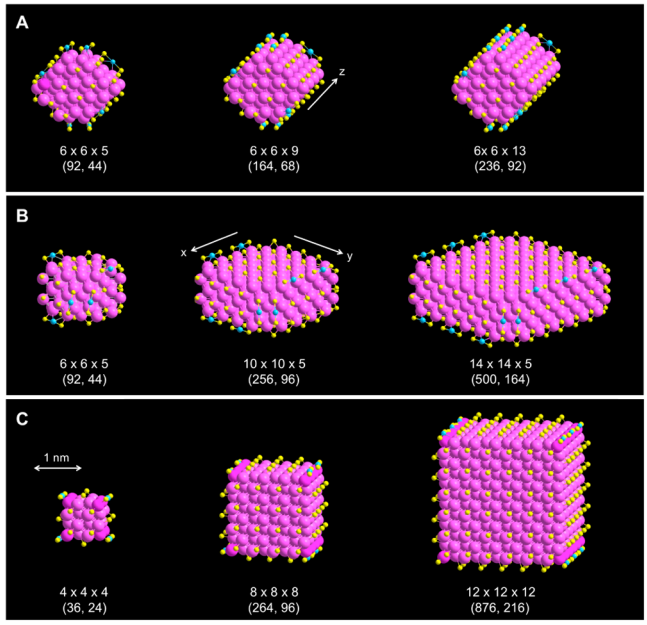

Figure 4. Tetragonal-shaped $Au_n(SR)_m$ nanocrystals constructed based on the $Au_{92}(TBBT)_{44}$ structure: (A) growth along the z direction to form 1D rods; (B) growth along x and y directions to form 2D plates; (C) growth along x, y, and z directions to form 3D cubes.

plates with the (n, m) value of $(2.5k^2 + k - 4, 0.5k^2 + 5k - 4)$ (Figure 4B). (iii) The nanocrystal grows by 3D expansion, which leads to cubic structures following the formula of $(0.5k^3 + k, 1.5k^2)$ (Figure 4C). The starting nanocrystal in the cube family is a 4 × 4 × 4 cube formulated as $Au_{36}(SR)_{24}$, which is actually identical to the previously discovered structures.[26] Also, in this way, the 6 × 6 × 5 Au_{92} nanocrystal can be viewed as either a 3D expansion of the 4 × 4 × 3 Au_{28} nanocrystal or a 2D expansion of the 4 × 4 × 5 Au_{44} nanocrystal (Figure S6).[27] These generalized structural models define a new category of faceted nanocrystals, as opposed to the staple-motif-based nonfaceted nanoclusters (e.g., spheres, spheroids, etc.).[10,11,18,19] The models are also important for understanding the facet development, shape control, and edge/corner effects in larger nanoparticles (e.g., >1000 gold atoms),[31−33] whose structures are by far still difficult to solve by X-ray crystallography.[34]

Compared with the self-assembly in the case of 2D surfaces, self-assembly in the 3D nanocrystals is more complicated due to the boundary effects, which lead to the discrete nature of sizes. It requires the number of the leftover gold atoms at the edge sites of the (100) facets being even, in order to fit the two sulfur atoms in one −S−Au−S− motif. Thus, the increment of layers progresses with a spacing of four in each expansion mode, for example, 4 × 4 × 4, 8 × 8 × 8, 12 × 12 × 12. It also provides an explanation to why two columns of atoms are truncated from the regular 6 × 6 × 5 lattice in $Au_{92}(TBBT)_{44}$; in this way, the three leftover gold atoms at the edge sites can be eliminated (Figure 1A, gray balls).

The atomic structure of $Au_{92}(TBBT)_{44}$ provides answers to the two open questions raised in the introduction: (i) the planar and curved surfaces follow different binding and patterning modes: the planar Au(100) facets in Au_{92} are protected by simple bridging thiolates and exhibit translational symmetry, as opposed to the curved surface, which is protected by staple motifs with rotational symmetry.[18,19] (ii) The edge and corner sites can be viewed as being protected, respectively,

DOI: 10.1021/jacs.6b04835
J. Am. Chem. Soc. 2016, 138, 8710−8713

by the monomeric and dimeric staple motifs, and they are the natural extension of the surface bridging thiolates, since the staple motifs can be decomposed into simple bridging units. This implies that the staple motifs are favored on the curved surface and at the edge/corner sites.

In regards to the potential sensitivity of SAM structure to the carbon tail of thiolate, we note that a comparison of our case of aromatic thiolate ligands (SPh-^{t}Bu) with the commonly used longchain alkanethiolates[28,29] such as $SC_{12}H_{25}$ indicates the same SAM structure.

Finally, it is worth noting that the structural mode of nanoSAMs observed in $Au_{92}(TBBT)_{44}$ does not reflect the defect effect in the general SAM structure since the facets on the nanocrystals are free of defects but the general surface contains defect sites such as terraces, ledges, kinks, and vacancies,[35] which may provide "adatoms" for formation of Au−S staple motifs. Nevertheless, the nanocrystal system still provides important information for understanding the potentially more complicated self-assembly behavior on bulk surfaces. In addition, different binding geometry may be presented on different crystalline surfaces such as Au{111}. We envision that by tuning of the ligand's structure[36] different crystalline facets on the nanocrystals would be stabilized, in order to achieve comprehensive knowledge on different SAMs (e.g., {111} and {110}), as well as the formation mechanisms of shape-controlled nanoparticles. The Au−S interaction model will further provide precise understanding of gold−thiolate based 2D nanotechnology.

■ ASSOCIATED CONTENT

Supporting Information

The Supporting Information is available free of charge on the ACS Publications website at DOI: 10.1021/jacs.6b04835.

Details of the synthesis, crystallization and X-ray analysis, and supporting Figures S1−6, Table S1−2. (PDF)

Crystallographic structure of the $Au_{92}(TBBT)_{44}$ (CIF)

■ AUTHOR INFORMATION

Corresponding Author

*rongchao@andrew.cmu.edu

Notes

The authors declare no competing financial interest.

■ ACKNOWLEDGMENTS

R.J. acknowledges support from the Air Force Office of Scientific Research under AFOSR Award No. FA9550-15-1-9999 (FA9550-15-1-0154) and the Camille Dreyfus Teacher-Scholar Awards Program. We thank Dr. Zhongrui Zhou for assistance in ESI-MS analysis.

■ REFERENCES

(1) Love, J. C.; Estroff, L. A.; Kriebel, J. K.; Nuzzo, R. G.; Whitesides, G. M. *Chem. Rev.* **2005**, *105*, 1103.

(2) Piner, R. D.; Zhu, J.; Xu, F.; Hong, S.; Mirkin, C. A. *Science* **1999**, *283*, 661.

(3) Thomas, J. C.; Boldog, I.; Auluck, H. S.; Bereciartua, P. J.; Dušek, M.; Macháček, J.; Bastl, Z.; Weiss, P. S.; Baše, T. *Chem. Mater.* **2015**, *27*, 5425.

(4) Heimel, G.; Romaner, L.; Zojer, E.; Bredas, J.-L. *Acc. Chem. Res.* **2008**, *41*, 721.

(5) Vericat, C.; Vela, M. E.; Benitez, G.; Carro, P.; Salvarezza, R. C. *Chem. Soc. Rev.* **2010**, *39*, 1805.

(6) Nuzzo, R. G.; Allara, D. L. *J. Am. Chem. Soc.* **1983**, *105*, 4481.

(7) Ulman, A. *Chem. Rev.* **1996**, *96*, 1533.

(8) Schreiber, F. *Prog. Surf. Sci.* **2000**, *65*, 151.

(9) Häkkinen, H. *Nat. Chem.* **2012**, *4*, 443.

(10) Jin, R. *Nanoscale* **2015**, *7*, 1549.

(11) Jadzinsky, P. D.; Calero, G.; Ackerson, C. J.; Bushnell, D. A.; Kornberg, R. D. *Science* **2007**, *318*, 430.

(12) Cossaro, A.; Mazzarello, R.; Rousseau, R.; Casalis, L.; Verdini, A.; Kohlmeyer, A.; Floreano, L.; Scandolo, S.; Morgante, A.; Klein, M. L.; Scoles, G. *Science* **2008**, *321*, 943.

(13) Maksymovych, P.; Yates, J. T. *J. Am. Chem. Soc.* **2008**, *130*, 7518.

(14) Pei, Y.; Gao, Y.; Shao, N.; Zeng, X. C. *J. Am. Chem. Soc.* **2009**, *131*, 13619.

(15) Jiang, D.-e. *Chem. - Eur. J.* **2011**, *17*, 12289.

(16) Das, A.; Li, T.; Nobusada, K.; Zeng, C.; Rosi, N. L.; Jin, R. *J. Am. Chem. Soc.* **2013**, *135*, 18264.

(17) Zeng, C.; Liu, C.; Chen, Y.; Rosi, N. L.; Jin, R. *J. Am. Chem. Soc.* **2014**, *136*, 11922.

(18) Chen, Y.; Zeng, C.; Liu, C.; Kirschbaum, K.; Gayathri, C.; Gil, R. R.; Rosi, N. L.; Jin, R. *J. Am. Chem. Soc.* **2015**, *137*, 10076.

(19) Zeng, C.; Chen, Y.; Kirschbaum, K.; Appavoo, K.; Sfeir, M. Y.; Jin, R. *Sci. Adv.* **2015**, *1*, e1500045.

(20) Poirier, G. E.; Pylant, E. D. *Science* **1996**, *272*, 1145.

(21) Voznyy, O.; Dubowski, J. J.; Yates, J. T.; Maksymovych, P. *J. Am. Chem. Soc.* **2009**, *131*, 12989.

(22) Luedtke, W. D.; Landman, U. *J. Phys. Chem.* **1996**, *100*, 13323.

(23) Bourg, M.-C.; Badia, A.; Lennox, R. B. *J. Phys. Chem. B* **2000**, *104*, 6562.

(24) Templeton, A. C.; Wuelfing, W. P.; Murray, R. W. *Acc. Chem. Res.* **2000**, *33*, 27.

(25) Whetten, R. L.; Price, R. C. *Science* **2007**, *318*, 407.

(26) Zeng, C.; Qian, H.; Li, T.; Li, G.; Rosi, N. L.; Yoon, B.; Barnett, R. N.; Whetten, R. L.; Landman, U.; Jin, R. *Angew. Chem., Int. Ed.* **2012**, *51*, 13114.

(27) Zeng, C.; Chen, Y.; Iida, K.; Nobusada, K.; Kirschbaum, K.; Lambright, K. J.; Jin, R. *J. Am. Chem. Soc.* **2016**, *138*, 3950.

(28) Dubois, L. H.; Zegarski, B. R.; Nuzzo, R. G. *J. Chem. Phys.* **1993**, *98*, 678.

(29) Sellers, H.; Ulman, A.; Shnidman, Y.; Eilers, J. E. *J. Am. Chem. Soc.* **1993**, *115*, 9389.

(30) Zeng, C.; Chen, Y.; Liu, C.; Nobusada, K.; Rosi, N. L.; Jin, R. *Sci. Adv.* **2015**, *1*, e1500425.

(31) Xia, Y.; Xiong, Y.; Lim, B.; Skrabalak, S. E. *Angew. Chem., Int. Ed.* **2009**, *48*, 60.

(32) Personick, M. L.; Mirkin, C. A. *J. Am. Chem. Soc.* **2013**, *135*, 18238.

(33) Ye, X.; Chen, J.; Engel, M.; Millan, J. A.; Li, W.; Qi, L.; Xing, G.; Collins, J. E.; Kagan, C. R.; Li, J.; Glotzer, S. C.; Murray, C. B. *Nat. Chem.* **2013**, *5*, 466.

(34) (a) Wilson, N. T.; Johnston, R. L. *Phys. Chem. Chem. Phys.* **2002**, *4*, 4168. (b) Barnard, A. S. *Cryst. Growth Des.* **2013**, *13*, 5433. (c) Djebaili, T.; Richardi, J.; Abel, S.; Marchi, M. *J. Phys. Chem. C* **2015**, *119*, 21146.

(35) Grumelli, D.; Maza, F. L.; Kern, K.; Salvarezza, R. C.; Carro, P. *J. Phys. Chem. C* **2016**, *120*, 291.

(36) (a) Chen, Y.; Zeng, C.; Kauffman, D. R.; Jin, R. *Nano Lett.* **2015**, *15*, 3603. (b) Chen, Y.; Liu, C.; Tang, Q.; Zeng, C.; Higaki, T.; Das, A.; Jiang, D.-e.; Rosi, N. L.; Jin, R. *J. Am. Chem. Soc.* **2016**, *138*, 1482. (c) Higaki, T.; Liu, C.; Zeng, C.; Jin, R.; Chen, Y.; Rosi, N. L.; Jin, R. *Angew. Chem., Int. Ed.* **2016**, *55*, 6694.

DOI: 10.1021/jacs.6b04835
J. Am. Chem. Soc. 2016, 138, 8710−8713